Biofilm Elimination



Rapid Biofilm Elimination on Bone Implants Using **Near-Infrared-Activated Inorganic Semiconductor** Heterostructures

Li Hong, Xiangmei Liu,* Lei Tan, Zhenduo Cui, Xianjin Yang, Yangin Liang, Zhaoyang Li, Shengli Zhu, Yufeng Zheng, Kelvin Wai Kwok Yeung, Doudou Jing, Dong Zheng, Xianbao Wang, and Shuilin Wu*

Bacterial infections often cause orthopedic surgery failures. It is hard for the immune system and antibiotics to clear bacteria adhered to implants after they form a mature biofilm, and a secondary surgery is required to remove the infected implants. To avoid this, a hybrid coating of Bi₂S₃@Ag₃PO₄/Ti is prepared to eliminate biofilm using near-infrared (NIR) light. Bi₂S₃ nanorod (NR) arrays are prepared on titanium (Ti) implants through hydrothermal methods, and Ag₃PO₄ nanoparticles (NPs) are loaded on Bi₂S₃ NR arrays using a stepwise electrostatic adsorption strategy. The introduction of Ag₃PO₄ NPs enhances the photocatalysis performances of Bi₂S₃, and the hybrid coating also exhibits good photothermal effects. After 808 nm light irradiation for 15 min, it shows superior bactericidal efficiency of 99.45% against Staphylococcus aureus, 99.74% against Escherichia coli in vitro, and 94.54% against S. aureus biofilm in vivo. Bi₂S₃@Ag₃PO₄/Ti also shows good cell viability compared to pure Ti. This NIRactivated-inorganic hybrid semiconductor heterojunction coating is biocompatible and could be employed to eliminate biofilm effectively, which makes it a very promising strategy for the surface modification of bone implant materials.

1. Introduction

The failure of orthopedic implantation surgery because of bacterial infection is very common.^[1] Although the surgical environment is strictly sterilized, pathogenic bacteria are unavoidable, and it is possible for them to adhere to implants. Traditional treatment requires repeated and long-term intravenous or oral antibiotics, which can damage the immunologic system and may also lead to bacterial resistance.^[2] Furthermore, if the bacteria attached to the material surface are not removed in time, they can multiply in large quantity to form a biofilm and secrete polysaccharides, which protect them from antibiotics and the immune system.^[3] This outcome necessitates a second surgery to remove the infected implants and means that patients suffer additional physical pain and financial loss.[4]

Photodynamic therapy (PDT) introduced by reactive oxygen species (ROS) has been widely studied in sterilization.^[5] ROS produced by a photodynamic system can kill cells in a short time.^[6] Compared to ultraviolet and visible (vis) light, near-

infrared (NIR) light possesses deeper biological tissue penetration ability, causes minimal photodamage to living bodies, and has been widely used in phototherapy.^[7] As demonstrated by Faris et al., [8] the effective penetration depth of NIR into a neonatal head could be several millimeters, so biofilm infections

Dr. L. Hong, Prof. X. Liu, Dr. L. Tan, Prof. X. Wang Ministry of Education Key Laboratory for the Green Preparation and Application of Functional Materials

Hubei Key Laboratory of Polymer Materials School of Materials Science and Engineering

Hubei University Wuhan 430062, China

E-mail: liuxiangmei1978@163.com

Prof. Z. Cui, Prof. X. Yang, Prof. Y. Liang, Prof. Z. Li, Prof. S. Zhu,

School of Materials Science and Engineering

The Key Laboratory of Advanced Ceramics and Machining

Technology by the Ministry of Education of China

Tianiin University Tianjin 300072, China E-mail: shuilinwu@tju.edu.cn

can be found under https://doi.org/10.1002/adhm.201900835.

The ORCID identification number(s) for the author(s) of this article

State Key Laboratory for Turbulence and Complex System and

Department of Materials Science and Engineering

College of Engineering **Peking University** Beijing 100871, China

Dr. K. W. K. Yeung

Department of Orthopaedics and Traumatology

Li KaShing Faculty of Medicine The University of Hong Kong Pokfulam, Hong Kong 999077, China

Dr. D. Jing, Prof. D. Zheng Department of Orthopaedics Union Hospital

Tongji Medical College

Huazhong University of Science and Technology

Wuhan 430022, China

DOI: 10.1002/adhm.201900835

www.advhealthmat.de

of artificial knee joints, skulls, elbow joints, and knuckles implanted under the skin could be treated by NIR phototherapy. Recent research by Wu and co-workers, [9] led to the development of a photoresponsive antibiofilm coating composed of organic photosensitizer IR780 iodide and inorganic semiconductor photothermal agent molybdenum disulfide (MoS₂). The Staphylococcus aureus biofilm on the implants was eradicated within 20 min under NIR light due to the combined action of PDT, photothermal therapy (PTT), and glutathione oxidation. However, using IR780 as the photosensitizer often suffers from poor stability and lack of bacteriostatic effect under dark conditions.[10] In comparison, inorganic semiconductors with high stability can be used as a ROS generator for PDT. Using NIRactivated semiconductors as a coating strategy combines rapid biofilm elimination capacity with long-term antimicrobial effect is a promising surface modification for implant materials.

Bismuth sulfide (Bi₂S₃) is a promising photocatalyst with a narrow bandgap (1.3-1.7 eV). Owing to its large absorption coefficient (104-105 cm-1) and high photoconductivity,[11] this abundant material has been widely used in the field of photodegradation of photovoltaic cells, photodetectors, and organic dyes.[12] The good biocompatibility and high photothermal conversion efficiency of Bi₂S₃ lends itself to wide application in the biomedical field. $^{[13]}$ Theoretically, $\mathrm{Bi}_2\mathrm{S}_3$ can generate electrons and holes under NIR light, and they can react with surrounding water or oxygen to produce ROS. Bi₂S₃ also provides an additional advantage of photothermal properties that help kill bacteria, which is different from some other bismuth-based semiconductors, such as bismuth oxychloride (BiOCl).^[14] Nevertheless, Bi₂S₃ is rarely employed singly in photocatalytic reactions because of the severe recombination of its photogenerated carriers.

Recent studies have focused on the combination of narrow bandgap semiconductors with the wider one to promote light absorption and increase the speed of charge separation, and in turn, improve the photocatalytic effect.^[15] Among the photocatalysts under investigation, trisilver phosphate (Ag₃PO₄), has a bandgap of 2.36 eV, possesses good bacteriostatic properties, and expresses low toxicity to mammalian cells, making it a potential antimicrobial material in vivo.[16] Therefore, Bi₂S₃ NR arrays grown on Ti implants were combined with Ag₃PO₄ NPs to achieve higher photocatalytic effects and rapid biofilm elimination, and relevant mechanisms are discussed in the paper. Bi₂S₃ NR arrays were grown on Ti implants through hydrothermal methods, and Ag₃PO₄ nanoparticles (NPs) were loaded onto Bi₂S₃ NR arrays using a stepwise electrostatic adsorption strategy. Based on the synergistic therapy of PDT and PTT under an 808 nm NIR light, this coating on the Ti plates was expected to accomplish biofilm elimination within 15 min. This was expected to work better than general phototherapy strategies like bismuth ferrite (Bi_{2.88}Fe₅O₁₂),^[17] because the trace amount of silver (Ag) ions released from the coating enabled it an effective bacteriostatic action in the absence of light. To the best of our knowledge, this type of coating on bone implants, composed of NIR-triggered inorganic semiconductor heterojunction photocatalysts, has not been reported yet. The hybrid semiconductor heterojunction coating, with efficient biofilm elimination and good cell activity, is encouraging for the future of antimicrobial coatings building on bone implant surfaces.

2. Results and Discussion

2.1. Synthesis and Characterizations of Bi_2S_3/Ti and $Bi_2S_3 @ Ag_3PO_4/Ti$

The schematic of the synthesis procedure for the Bi₂S₃@ Ag₃PO₄ NR arrays on Ti plates is illustrated in Figure 1. The alkali-treated Ti plates with a network-like surface showed homogeneous distribution of "S" element of 4-mercaptobenzoic acid (4-MBA) (Figure S1a,b, Supporting Information). Bi₂S₃ NR arrays were derived from an aqueous solution at 50 °C on the 4-MBA-treated Ti plate. Figure 2a,b shows sharp-tip Bi₂S₃ NRs grown densely and homogeneously on the surface of Ti plates. After being compounded with Ag₃PO₄, the coating remained intact (Figure 2c), but the surface of Bi₂S₃ NR arrays was coated by Ag₃PO₄ NPs with an average size of 21.1 \pm 0.2 nm (Figure 2d). Meanwhile, Ag₃PO₄ grown in solution had a larger and more heterogeneous particle size of 420 ± 2 nm (Figure S2, Supporting Information). The reduced Ag₃PO₄ particle size was ascribed to the space-confined effect of Bi₂S₃ hierarchical nanorods. [18] Transmission electron microscope (TEM) images showed that Bi₂S₃ NRs were subuliform (Figure 2e), which was identical to the scanning electron microscope (SEM) observation in Figure 2b. The lattice fringe of 0.40, 0.36, and 0.31 nm located on the high-resolution image (Figure 2f) was indexed to the planes (220), (130), and (211) of Bi₂S₃ (JCPDS Card File No. 17-0320, orthorhombic lattice). [19] The inset image in Figure 2f disclosed that the fast Fourier transform (FFT) pattern (corresponding to the red rectangle) affirmed the existence of the Bi₂S₃ crystal, which showed planes (130) of 0.36 nm d-spacing and (211) of 0.35 nm. After treatment with AgNO₃ and Na2HPO4 solutions successively, the formed NPs were wrapped around Bi₂S₃ NR arrays (Figure 2g) and the highresolution image (Figure 2h) and FFT pattern (corresponding to the red rectangle in the Figure 2h inset) showed the coexistence of Ag₃PO₄ and Bi₂S₃. The former showed planes (200) and (211) with corresponding spacing of 0.30 and 0.25 nm (JCPDS Card File No. 06-0505, body-centered cubic), [15a] while the latter exhibited planes of (211) and (310) with spacing of 0.31 and 0.35 nm (JCPDS Card File No. 17-0320, orthorhombic lattice). The results revealed the compact contact interface between Bi₂S₃ and Ag₃PO₄. Energy-dispersive X-ray spectroscopy (EDS) mapping disclosed the uniform distribution of Bi, S, Ag, P, and O in Bi₂S₃@Ag₃PO₄ NRs (Figure S3, Supporting Information). Cross-section images in Figure S4a (Supporting Information)

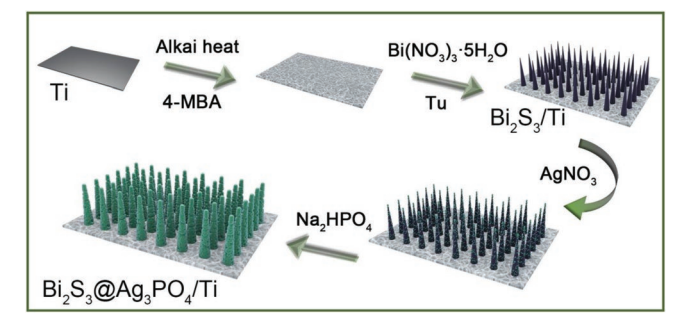


Figure 1. Illustration for the synthesis procedures for $Bi_2S_3@Ag_3PO_4$ nanorod arrays on Ti plates.

www.advhealthmat.de

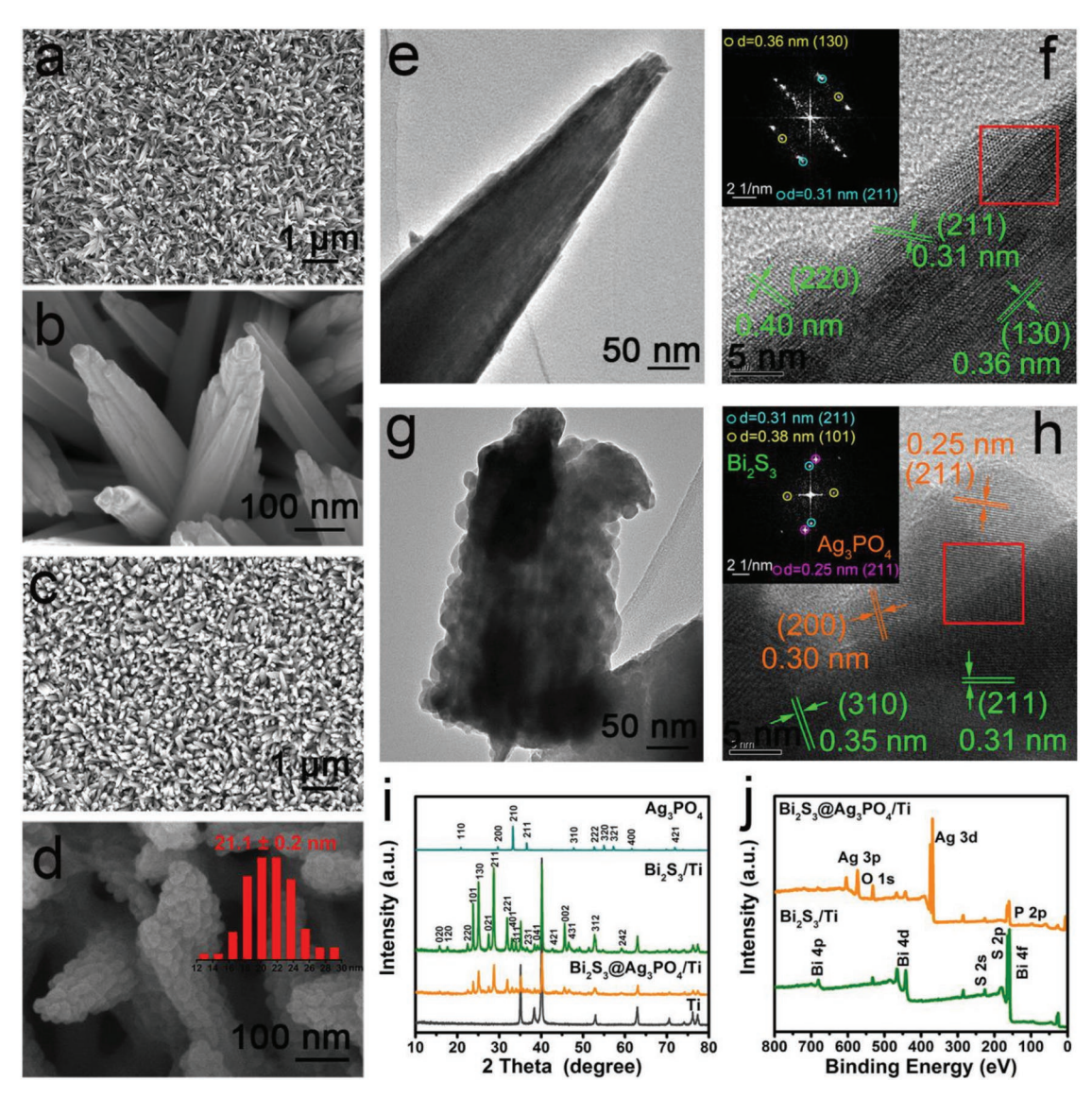


Figure 2. FESEM images of a,b) Bi_2S_3/Ti and c,d) $Bi_2S_3 @ Ag_3PO_4/Ti$. TEM and HRTEM images of e,f) Bi_2S_3 and g,h) $Bi_2S_3 @ Ag_3PO_4$ separated from Bi_2S_3/Ti and $Bi_2S_3 @ Ag_3PO_4/Ti$, respectively (inset FFT patterns are corresponding to the red rectangle). i) XRD patterns. j) XPS spectra.

show that the ${\rm Bi_2S_3@Ag_3PO_4}$ coating was about 2 μm thick. Elemental line scanning (Figure S4b, Supporting Information) and mapping images (Figure S4c, Supporting Information) indicated the homogeneous distribution of Bi, S, Ag, P, and O in the coating.

The phase compositions and chemical compositions of $Bi_2S_3@Ag_3PO_4/Ti$ were further determined by X-ray powder diffraction (XRD) and X-ray photoelectron spectroscopy (XPS). As shown in Figure 2i, the lattice planes (110), (210), and (211) of Ag_3PO_4 powder, prepared using the same methods as the coating, were fully consistent with body-centered cubic structure of Ag_3PO_4 (JCPDS Card File No. 06-0505). [16a] The $Bi_2S_3@Ag_3PO_4/Ti$ composites showed almost the same diffraction peaks with different peak intensities as the Bi_2S_3/Ti , which was readily indexed to the orthorhombic lattice of Bi_2S_3 (JCPDS Card File No. 17-0320), [19] except for the diffraction peaks from pure Ti. The result illustrated that the structure of Bi_2S_3

phase was unchanged after modification with Ag₃PO₄ NPs.^[20] The Ag₃PO₄ signal was not detected in the XRD pattern of Bi₂S₃@Ag₃PO₄/Ti due to its low content in the composite.^[21] The XPS survey scan (Figure 2j) indicated that the surface of Bi₂S₃@Ag₃PO₄/Ti included Bi, S, Ag, P, and O elements, while pure Bi₂S₃/Ti was composed of Bi and S. Figure S5a (Supporting Information) shows the high-resolution Bi 4f and S 2p spectra, with peaks at 163.9 and 158.6 eV in Bi₂S₃/ Ti, and at 164.8 and 159.5 eV in Bi₂S₃@Ag₃PO₄/Ti. These corresponded to Bi 4f5/2 and Bi 4f7/2. The peaks at 162.5 and 161.3 eV in Bi₂S₃/Ti and Bi₂S₃@Ag₃PO₄/Ti were attributed to S2p1/2 and S2p3/2, respectively.^[22] The Bi 4f peaks in Bi₂S₃@ Ag₃PO₄/Ti shifted toward higher binding energy compared to those in Bi₂S₃/Ti, which was attributed to the strong bond between Bi₂S₃ and Ag₃PO₄ because of the electronic shielding effect.^[23] A slight drop of the Bi peak in Bi₂S₃@Ag₃PO₄/Ti compared to Bi₂S₃/Ti was due to the partial, rather than full,

ADVANCED HEALTHCARE MATERIALS

coverage of Ag_3PO_4 NPs, because the Ag_3PO_4 NP diameter was greater than the XPS penetration depth. The binding energy located at 374.2 and 368.2 eV in Figure S5b (Supporting Information) was ascribed to Ag 3d3/2 and Ag 3d5/2, respectively, as was characteristic of $Ag^+.[^{24}]$ There was no evidence showing the existence of other valence states of the Ag element, which was consistent with Figure 2h. The binding energy value of P 2p (Figure S5c, Supporting Information) and O 1s (Figure S5d, Supporting Information) was 133.1 and 531.0 eV, respectively, indicating the existence of phosphorus (P^{5+}) and lattice oxygen in $Ag_3PO_4.^{[25]}$

2.2. Photodynamic and Photothermal Properties

The UV-vis diffuse reflectance spectroscopy (DRS) spectra of different samples were tested to evaluate optical properties.

According to **Figure 3**a, pure Ti showed poor capability to absorb light from 300 to 1200 nm wavelengths and Bi_2S_3/Ti displayed a strong absorption peak centered at 800 nm, whereas Ag_3PO_4 showed stronger absorption capacity for vis light than NIR light (inset image in Figure 3a). However, the integration of Ag_3PO_4 with Bi_2S_3 not only made a redshift of the characteristic absorption peak of silver phosphate but also enhanced the absorption capacity of Bi_2S_3/Ti over the entire spectrum (300–1200 nm), indicating that $Bi_2S_3@Ag_3PO_4/Ti$ possessed superior light absorption ability than Bi_2S_3/Ti or Ag_3PO_4 separately. Figure 3b was the bandgap diagram of different samples, and the bandgap can be calculated using the following equation P_3 0.

$$(\alpha h v)^n = C(h v - E_g) \tag{1}$$

From the Tauc plot, the bandgap of Bi₂S₃/Ti decreased from 1.37 to 1.32 eV with the addition of Ag₃PO₄, NPs. For Ag₃PO₄,

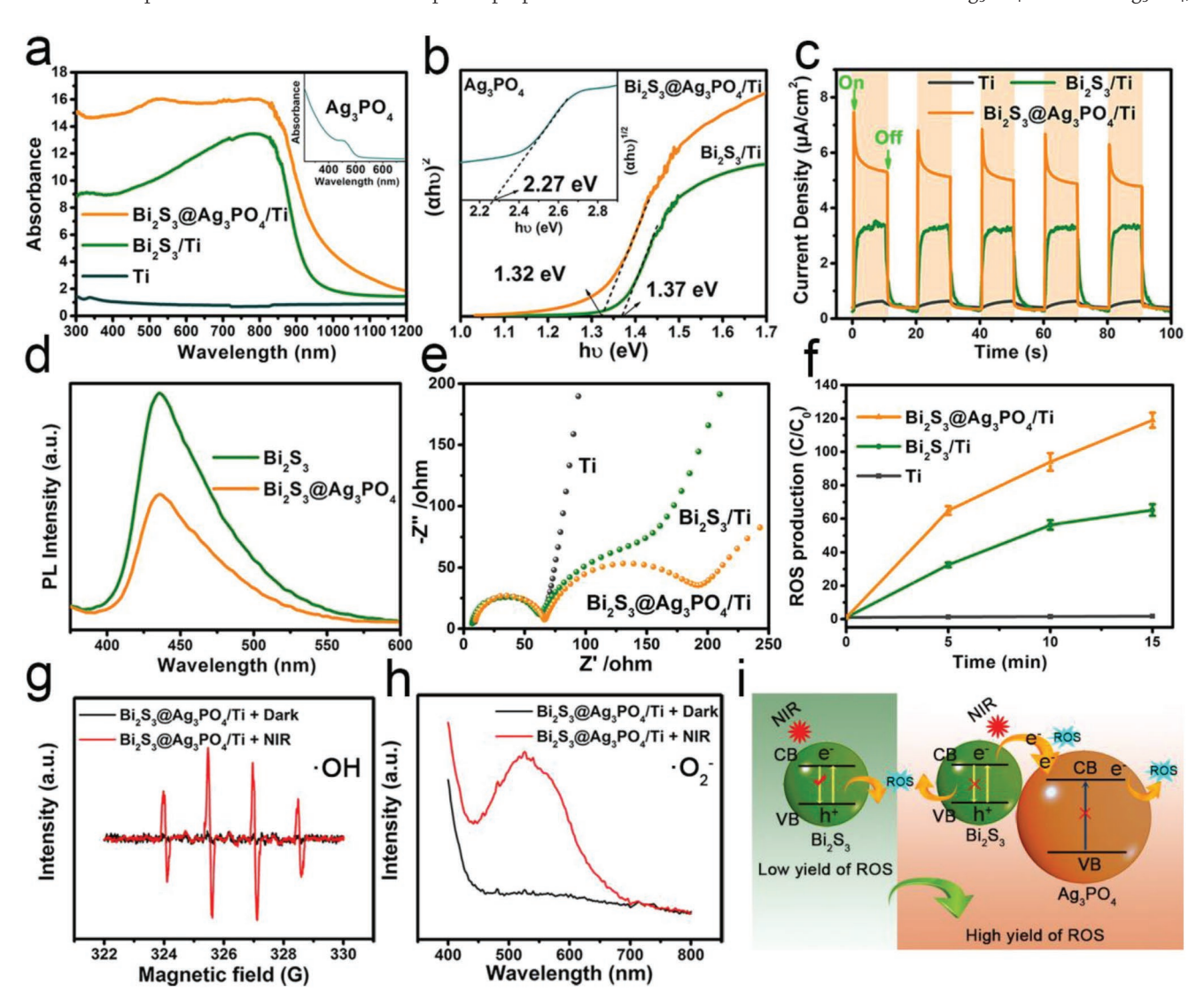


Figure 3. a) UV–vis DRS spectra and b) corresponding Tauc plot. c) Photocurrent response curves and d) PL spectra of Bi_2S_3 and Bi_2S_3 @Ag₃PO₄ solution prepared with powder scraped from Bi_2S_3 /Ti and Bi_2S_3 @Ag₃PO₄/Ti, respectively. e) EIS spectra of the photocatalysts under 808 nm NIR light irradiation. f) ROS production (the error bars represent means \pm SD, n = 3). g) ESR spectra of hydroxyl radicals. h) Superoxide radicals detected by NBT methods. i) The diagram of band alignment of Bi_2S_3 and Ag_3PO_4 and mechanism of ROS production before and after combination.



www.advhealthmat.de

ADVANCED HEALTHCARE MATERIALS

the indirect bandgap was calculated as 2.27 eV (inset curve in Figure 3b), indicating that pure Ag_3PO_4 could not be excited by the 808 nm laser. However, the modification of Ag_3PO_4 on Bi_2S_3/Ti broadened the band edge absorption of Bi_2S_3/Ti from 940 to 1000 nm.

The ability to absorb light is important for enhancing photocatalytic reactions, whereas the separation and transfer efficiency of photoinduced electrons and holes is critical in determining the photocatalytic properties of materials. The promoted charge separation capacity of Bi₂S₃@Ag₃PO₄/Ti compared to both Bi₂S₃/Ti and pure Ti was determined by the enhanced photocurrent density under 808 nm NIR light illumination. As displayed in Figure 3c, Bi₂S₃@Ag₃PO₄/Ti exhibited the highest photocurrent response among three kinds of samples, indicating the rapid charge separation between Bi₂S₃ and Ag₃PO₄ and the lower recombination rate of photogenerated carriers, which was proven by the reduced photoluminescence (PL) intensity of Bi₂S₃@Ag₃PO₄ compared to Bi₂S₃ (Figure 3d). Generally, higher PL intensity means a stronger probability for photogenerated electron-hole pair recombination.^[27] The PL emission intensity of Bi₂S₃@Ag₃PO₄ weakened dramatically in comparison with that of Bi₂S₃, indicating suppression of photogenerated electron-hole recombination by the introduction of Ag₃PO₄. In addition, Ag₃PO₄ NPs accelerated the transfer of photoinspired electrons of Bi₂S₃/Ti, which was confirmed by the lowest impedance shown in Figure 3e. The first arc radius can be categorized as the resistance of platinum (Pt) counter electrode/electrolyte interface while the second arc radius can be assigned to the charge-transfer resistance of different samples.^[28] Obviously, Bi₂S₃@Ag₃PO₄/Ti had a smaller arc radius than Bi₂S₃/Ti with 808 nm NIR light illumination, indicating a faster photoinspired electron-hole pairs separation of Bi2S3@ Ag₃PO₄/Ti.

ROS is a strong oxidant with excellent bacteria-killing ability, with the reaction generated between the photogenerated charges and water or oxygen in the surrounding environment. A higher concentration of total ROS can lead to a lower bacterial survival rate, [29] and Bi₂S₃@Ag₃PO₄/Ti showed a maximum yield of total ROS under NIR light (Figure 3f); therefore, it was expected to have the best antimicrobial sterilization effect. Different reactive oxygen species were verified by electron spin resonance (ESR) spectroscopy and nitro tetrazolium blue chloride (NBT) methods.[30] The production of •OH was characterized by ESR in water with 5,5-dimethyl-1-pyrroline-Noxide (DMPO) as the spin-trapping agent, [31] and the generation of •O₂ could be detected by its characteristic reaction with NBT. [32] As shown in Figure 3g,h, both •OH and •O₂ could be detected from Bi₂S₃@Ag₃PO₄/Ti samples under 808 nm NIR light illumination. Beyond that, both Bi₂S₃/Ti and Bi₂S₃@ Ag₃PO₄/Ti exhibited better photothermal effects in comparison with pure Ti, as observed in Figure S6a (Supporting Information). After immersion in 200 µL phosphate-buffered saline (PBS) solution, the surface temperature of Bi₂S₃@Ag₃PO₄/Ti increased from 17 to 52.4 °C within 3 min under the illumination of 0.5 W cm⁻² 808 nm NIR light, followed by Bi₂S₃/ Ti (17 to 50.4 °C) and pure Ti (17 to 37 °C). The evolution of surface temperature compared to irradiation time was directly observed by thermal images shown in Figure S6b (Supporting Information).

2.3. Photocatalytic Mechanism

The above results revealed that Bi₂S₃@Ag₃PO₄ was a typical type II heterostructure as illustrated in Figure 3i. The construction of the heterojunction enhanced photocatalytic activity, as well as the total ROS yield of Bi₂S₃. Bi₂S₃ with a narrow bandgap of 1.37 eV could generate ROS under 808 nm NIR light irradiation, but it suffered from severe recombination of photogenerated electron-holes, leading to a low ROS yield. After having been covered with Ag₃PO₄ NPs, the hybrid semiconductor heterojunctions bandgap narrowed to 1.32 eV, which was beneficial to producing photogenerated charges. The photocatalytic performance was also improved dramatically. Since the conduction band (CB) potentials of Ag₃PO₄ were lower than Bi₂S₃,^[16a,19] it was inferred that photogenerated Bi₂S₃ electrons could be transferred to Ag₃PO₄ smoothly, and in turn, move to the surface, promoting the separation of photocarriers. The well-designed core-shell structure of Bi₂S₃@Ag₃PO₄ made a full close-knit interfacial contact between Bi₂S₃ and Ag₃PO₄, thus providing sufficient transport channels for photogenerated carriers and facilitating the separation of photogenerated electron-hole pairs from Bi₂S₃. In addition, the enlarged specific surface area introduced by Ag₃PO₄ NPs provided more active sites, which was constructive for the photocatalytic redox reaction. In this way, Bi₂S₃@Ag₃PO₄/Ti produced more total ROS compared to Bi₂S₃/Ti.

2.4. In Vitro Antibacterial Ability and Relative Mechanisms for Biofilm Elimination

The spread plate method was used to transfer and distribute bacteria to an agar plate evenly to count bacterial survival in different groups. The spread plate images (Figure S7a, Supporting Information) of the dark group (all samples cocultured with bacteria without light irradiation) showed no reduction of bacterial colonies compared to Ti, indicating that all samples, including Bi₂S₃@Ag₃PO₄/Ti, had no antibacterial efficacy in darkness within 15 min. Even under NIR light irradiation, pure Ti displayed no antibacterial performance. In contrast, after exposure to 808 nm NIR, the two groups of Bi₂S₃/Ti and Bi₂S₃@Ag₃PO₄/ Ti exhibited considerably fewer bacteria survival, especially for the latter group, indicating that Bi₂S₃@Ag₃PO₄/Ti had the best antibacterial efficacy. As shown in Figure 4a, with 15 min NIR light illumination, the calculated antibacterial efficacy of Bi₂S₃/Ti against S. aureus and Escherichia coli was 82.75 and 80.05%, respectively. However, Bi₂S₃@Ag₃PO₄/Ti exhibited a higher antimicrobial efficiency of 99.32 and 99.52% under the same conditions. The higher sterilization effect was ascribed to the enhanced photocatalytic performance, stronger NIR light absorption intensity, and quicker separation of photogenerated carriers, through the addition of Ag₃PO₄ NPs. In addition, the combination of Bi₂S₃ and Ag₃PO₄ suppressed Ag⁺ leaching from Ag₃PO₄, thus providing the coating a slow, long-term Ag⁺ release (Figure S7b, Supporting Information), which ensured that the implant materials had lasting protection from bacterial infection. As shown in Figure S7c (Supporting Information), after coculturing with Bi₂S₃@Ag₃PO₄/Ti for 24 h in darkness, 99.45% of S. aureus and 99.74% of E. coli were killed because

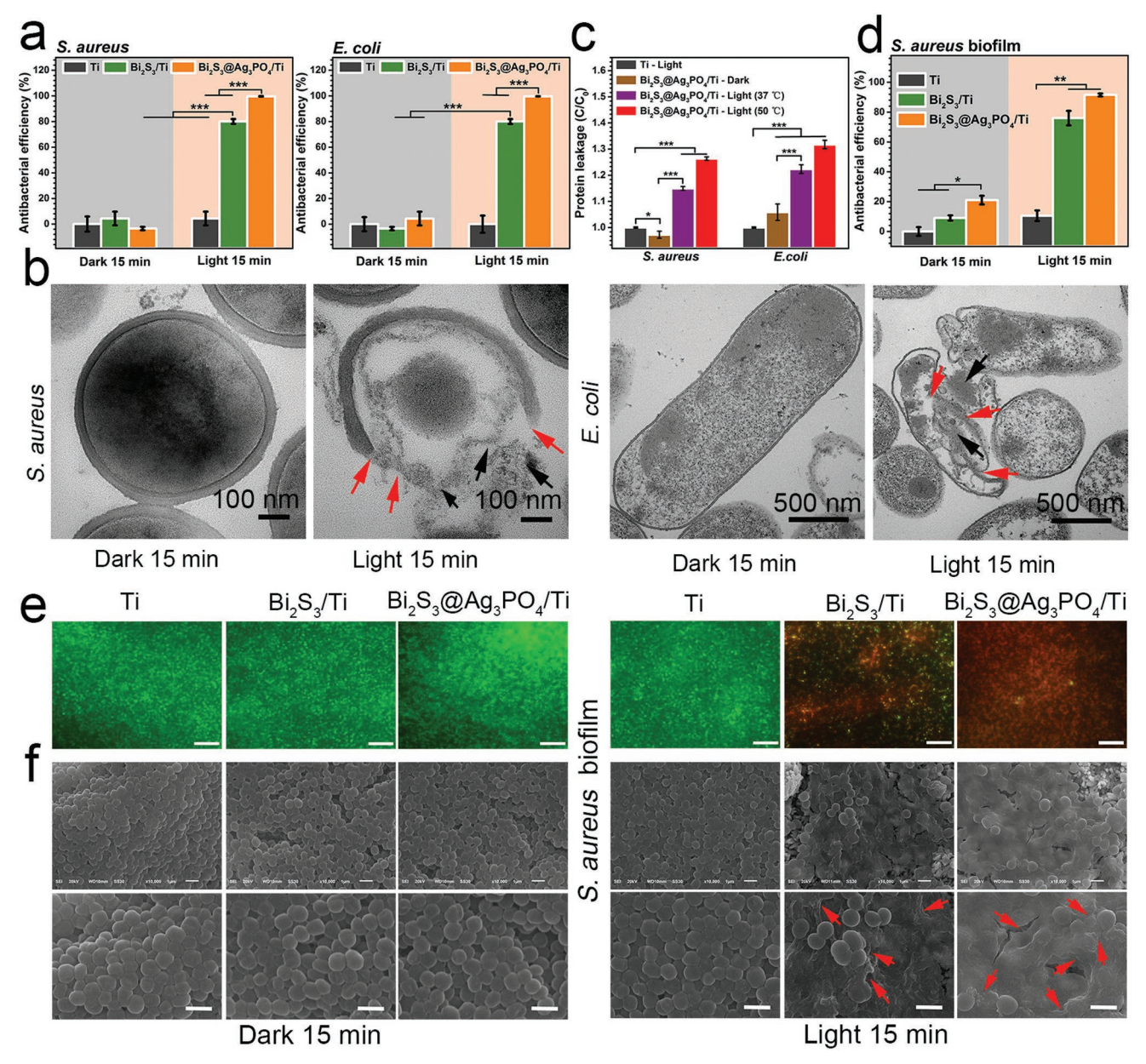


Figure 4. Antibacterial properties analysis in vitro. a) Antibacterial efficiency against *S. aureus* and *E. coli*. b) Protein leakage (OD_{562}). c) TEM images of the bacterial sections. d) Antibiofilm efficiency of the samples. e) Live/dead (green/red) staining fluorescence images (scale bar, 20 μm) and f) corresponding SEM images (scale bar, 1 μm) of *S. aureus* biofilm. The error bars represent means \pm SD, n = 3: *p < 0.05, **p < 0.01, ***p < 0.001.

of the broad-spectrum bactericidal properties of released Ag⁺. In addition, as shown in Figure S7d (Supporting Information), both Ti and $\rm Bi_2S_3@Ag_3PO_4/Ti$ at 50 °C for 15 min in the absence of light (the temperature was on account of an extra water bath) showed antibacterial efficiency below 20%, indicating that heat-accelerated release of Ag ions did not kill bacteria alone effectively within 15 min.

ROS destroyed bacteria cell membrane structures by interacting with organisms in the bacteria and then penetrating the cell membrane, leading to gradual oxidative damage and leakage of intracellular substances, especially proteins and DNA, thus killing bacteria completely.^[29a] TEM was employed to observe the membrane damage and intracellular bacteria structural change. As illustrated in Figure 4b, both *S. aureus*

and $E.\ coli$ in the dark group (Bi $_2$ S $_3$ @Ag $_3$ PO $_4$ /Ti, dark 15 min) remained in normal morphology with integrated intracellular substrate and smooth membranes, while the light group (Bi $_2$ S $_3$ @Ag $_3$ PO $_4$ /Ti, light 15 min) were distorted or obviously broken (red arrows), and even suffered loss of cytoplasmic or intracellular bacteria proteins.

Figure 4c shows the protein leakage compared to the light group of pure Ti (808 nm NIR, 37 °C, 15 min) from *S. aureus* and *E. coli* processed under different conditions. The dark group of Bi₂S₃@Ag₃PO₄/Ti displayed almost no difference from the control group, which meant the structure and composition of Bi₂S₃@Ag₃PO₄/Ti could not cause structural damage to bacteria in a short time. The light group of Bi₂S₃@Ag₃PO₄/Ti (37 °C, 15 min, the temperature was because of the power density

www.advhealthmat.de

and red in different ratios, whereas pure Ti remained green. In addition, $Bi_2S_3@Ag_3PO_4/Ti$ showed more red fluorescence than Bi_2S_3/Ti . These results suggested that $Bi_2S_3@Ag_3PO_4/Ti$ had the best antibiofilm performance due to the synergistic action of photothermal effect and enhanced photocatalytic properties.

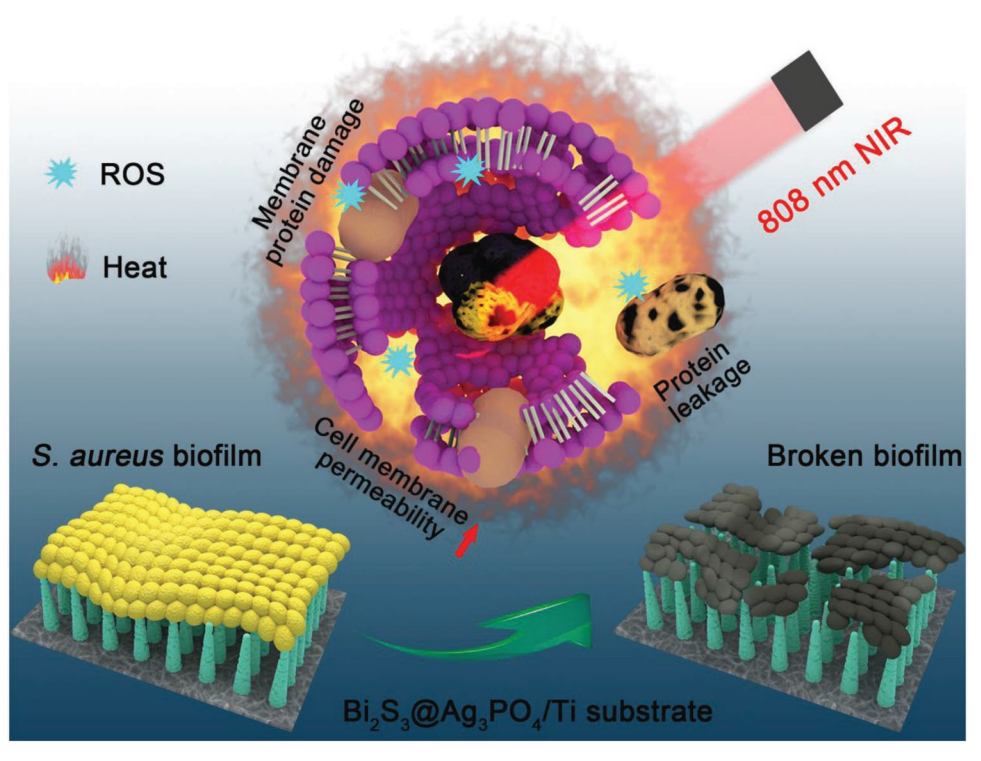
SEM was conducted to observe the morphology of biofilm and investigate the biofilm elimination mechanism. As shown in Figure 4f, the *S. aureus* biofilm, on the surfaces of the unilluminated Ti, ${\rm Bi}_2{\rm S}_3/{\rm Ti}$, ${\rm Bi}_2{\rm S}_3@{\rm Ag}_3{\rm PO}_4/{\rm Ti}$ and illuminated Ti, showed dense and intact cell walls with smooth surfaces. These meant that none of these samples including ${\rm Bi}_2{\rm S}_3@{\rm Ag}_3{\rm PO}_4/{\rm Ti}$ could inhibit the formation of *S. aureus* biofilm by themselves in the dark. In contrast, after exposure to NIR for 15 min, some of the cell walls were wrinkled and damaged (red arrow) on the surface of ${\rm Bi}_2{\rm S}_3/{\rm Ti}$ while the *S. aureus* biofilm on ${\rm Bi}_2{\rm S}_3@{\rm Ag}_3{\rm PO}_4/{\rm Ti}$ was almost wholly destroyed with several layers of collapsed, broken bacteria.

Based on the results above, the elimination mechanism of biofilm is proposed in **Scheme 1**. After 48 h coculture of samples and a high concentration bacterial solution, a mature *S. aureus* biofilm was formed on the surfaces of Bi₂S₃@ Ag₃PO₄/Ti. Under 808 nm NIR irradiation, Bi₂S₃@Ag₃PO₄/Ti generated ROS and local heat (50 °C) simultaneously. The hyperthermia produced by the coating under NIR increased the bacteria cell membrane permeability and caused membrane protein damage, accelerating ROS penetration into the cell membranes, which led to bacterial metabolic disorders and protein leakage. Suffering from the synergy of PDT and PTT, the inactivated bacteria increased as the time of illumination increases. After 15 min of phototherapy, the entire biofilm surface was broken.

of the 808 nm NIR laser and an extra water bath) exhibited 1.15-fold protein leakage of *S. aureus* compared to the control group while Bi₂S₃@Ag₃PO₄/Ti (50 °C, 15 min, the temperature was depended on the power density of the 808 nm NIR laser) showed that of 1.28-fold. Similar phenomena had been observed in *E. coli*. The results of protein leakage illustrated that the photothermal effect achieved sterilization by affecting the permeability of cell membranes, thus accelerating the ROS sterilization rate.

The results of antimicrobial tests against *S. aureus* and *E. coli*.

The results of antimicrobial tests against S. aureus and E. coli showed that Bi₂S₃@Ag₃PO₄/Ti had a good germicidal effect on normal bacteria in orthopedic infections. We then further studied the effect on elimination of biofilm, a more lethal infection in bone-implant-related surgery. Although Ag+ released from Bi₂S₃@Ag₃PO₄/Ti eliminated most normal bacteria within 24 h, S. aureus biofilm still formed on the surface of Bi₂S₃@ Ag₃PO₄/Ti in a high concentration bacterial solution, which is difficult to eliminate in traditional ways.[33] The viability of S. aureus biofilm was evaluated by spread plate and the qualitative live/dead staining assay. As shown in Figure S7e (Supporting Information) and Figure 4d-f, all samples including Bi₂S₃@Ag₃PO₄/Ti exhibited no obvious antibiofilm effects in darkness. In contrast, after 15 min NIR light irradiation, both Bi₂S₃/Ti and Bi₂S₃@Ag₃PO₄/Ti displayed obvious antibiofilm efficacy, especially for the latter, which owned 91.54% eradication of S. aureus biofilm. The fluorescence images of the dark group showed the green S. aureus (Figure 4e), indicating no obvious toxicity of samples including Bi₂S₃@Ag₃PO₄/Ti. S. aureus biofilm easily formed on the samples in the absence of light; however, after 15 min 808 nm NIR light irradiation, the Bi₂S₃/Ti and Bi₂S₃@Ag₃PO₄/Ti samples displayed both green



Scheme 1. The antibiofilm mechanism diagram of PDT and PTT induced by Bi₂S₃@Ag₃PO₄/Ti under 808 nm NIR light illumination toward bacteria.

ADVANCED HEALTHCARE

2.5. In Vitro Cell Activity

Fluorescein isothiocyanate (FITC) (green) and 4′,6-diamidino-2-phenylindole (DAPI) (blue) stains were used to visualize initial cell adhesion and spreading activity of cells qualitatively cocultured with different samples after 24 h. As shown in **Figure 5**a, Bi₂S₃/Ti and Bi₂S₃@Ag₃PO₄/Ti exhibited higher adhesion than pure Ti. The number and spreading area of cells on the surface of pure Ti was less than that of Bi₂S₃/Ti. Cells on Bi₂S₃/Ti extended a large number of fine filamentous pseudopodia, and the actin stress fibers had extended the complete cell morphology, while those on pure Ti were slender and spindle-shaped. Cells on Bi₂S₃@Ag₃PO₄/Ti showed a lower viability and spreading area than Bi₂S₃/Ti, owing to the cytotoxicity of a small amount of Ag⁺ released from Ag₃PO₄ to the cells, but it still exhibited good biocompatibility compared to pure Ti.

The methyl thiazolyl tetrazolium (MTT) method was used for quantitative analysis of sample biocompatibility. As seen in Figure 5b, Bi₂S₃/Ti and Bi₂S₃@Ag₃PO₄/Ti exhibited better biocompatibility than pure Ti after coculturing for 1, 3, and 7 d. Specifically, after coculturing for 1 d, the optical density (OD) of Bi₂S₃/Ti reached 1.2, and Bi₂S₃@Ag₃PO₄/Ti also had an OD value of 0.99 which was 0.29 higher than pure Ti. However, the cell density of Bi₂S₃@Ag₃PO₄/Ti decreased to 0.93 after 3 d culturing, while pure Ti was 0.89, which was ascribed to the toxicity of the trace amount of Ag+ released from Bi₂S₃@Ag₃PO₄/ Ti. However, the biological activity of Bi₂S₃@Ag₃PO₄/Ti was still superior to pure Ti after 7 d. Although Ag₃PO₄ NPs alone exhibited some toxicity due to the release of Ag⁺, [35] the strong electrostatic adsorption between Bi₂S₃ and Ag₃PO₄ suppressed the leaching of Ag+ from Bi₂S₃@Ag₃PO₄/Ti, which reduced the cytotoxicity of composite coatings. Meanwhile, Bi₂S₃ exhibited good biocompatibility, no residues in the organism were

reported,[36] and it has been widely applied in the biomedical field.^[13] In this work, the in vitro tests also demonstrated that Bi₂S₃/Ti showed good cell viability (see Figure 5a,b). Therefore, the excellent biocompatibility of Bi₂S₃ could offset the adverse effects of possible release of trace Ag+ amounts. The impact of NIR light on cell activities is shown in Figure S8 (Supporting Information). After 15 min of 808 nm NIR light illumination, followed by 1 d culturing, the cells on Bi₂S₂/Ti exhibited similar viability to those on Ti plates, indicating that the excellent biocompatibility of Bi₂S₃/Ti can offset the adverse effects caused by lower photothermal effect and less ROS production. However, under the same conditions, Bi₂S₃@Ag₃PO₄/Ti cell density decreased significantly, which was ascribed to the photothermal effect and a higher ROS yield compared to Bi₂S₃/Ti, as well as the released Ag ions. However, after 3 and 7 d of coculturing, both cells cocultured with Bi₂S₃/Ti and Bi₂S₃@Ag₃PO₄/Ti became normal, indicating that the effects of NIR light on cell viability could be ignored after recovery with a long period of incubation.

As shown in Figure 5c, both Bi_2S_3 /Ti and Bi_2S_3 @Ag₃PO₄/Ti exhibited promoted alkaline phosphatase (ALP) activity compared to pure Ti. In addition, the Bi_2S_3 @Ag₃PO₄/Ti showed the highest ALP expression because of the stimulus of the structure of nanorod arrays and moderate number of Ag ions. It has been reported that nanorod array structure can influence osteoblast behaviors. [37] Furthermore, a trace amount of Ag⁺ can also help to influence osteoblast behaviors to promote osteoblast differentiation. [38] The extent of extracellular matrix (ECM) mineralization was evaluated to further analyze osteogenic differentiation after 10 d culturing in osteogenic medium extracts. Quantitative measurement of mineralization (Figure 5d) showed the highest mineralization levels in cells on Bi_2S_3 @ Ag_3PO_4 /Ti, which was in accordance with Figure 5c.

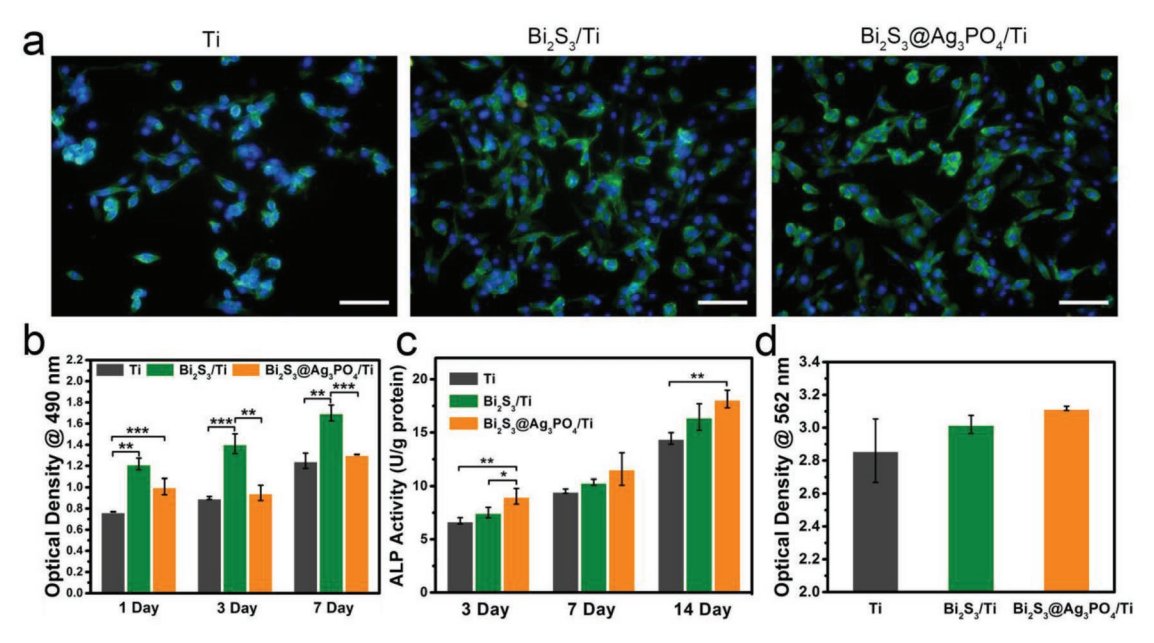


Figure 5. a) Fluorescence microscopy images of MC3T3-E1 cells cocultured with different samples after 24 h. The cytoskeletons were stained with FITC (green) and the nuclei were stained with DAPI (blue) (scale bar, 100 μ m). b) MTT assay and c) ALP activity. d) Quantitative measurement of the Alizarin Red staining after 10 d coculture. The error bars represent means \pm SD, n = 3: *p < 0.05, **p < 0.01, ***p < 0.001.

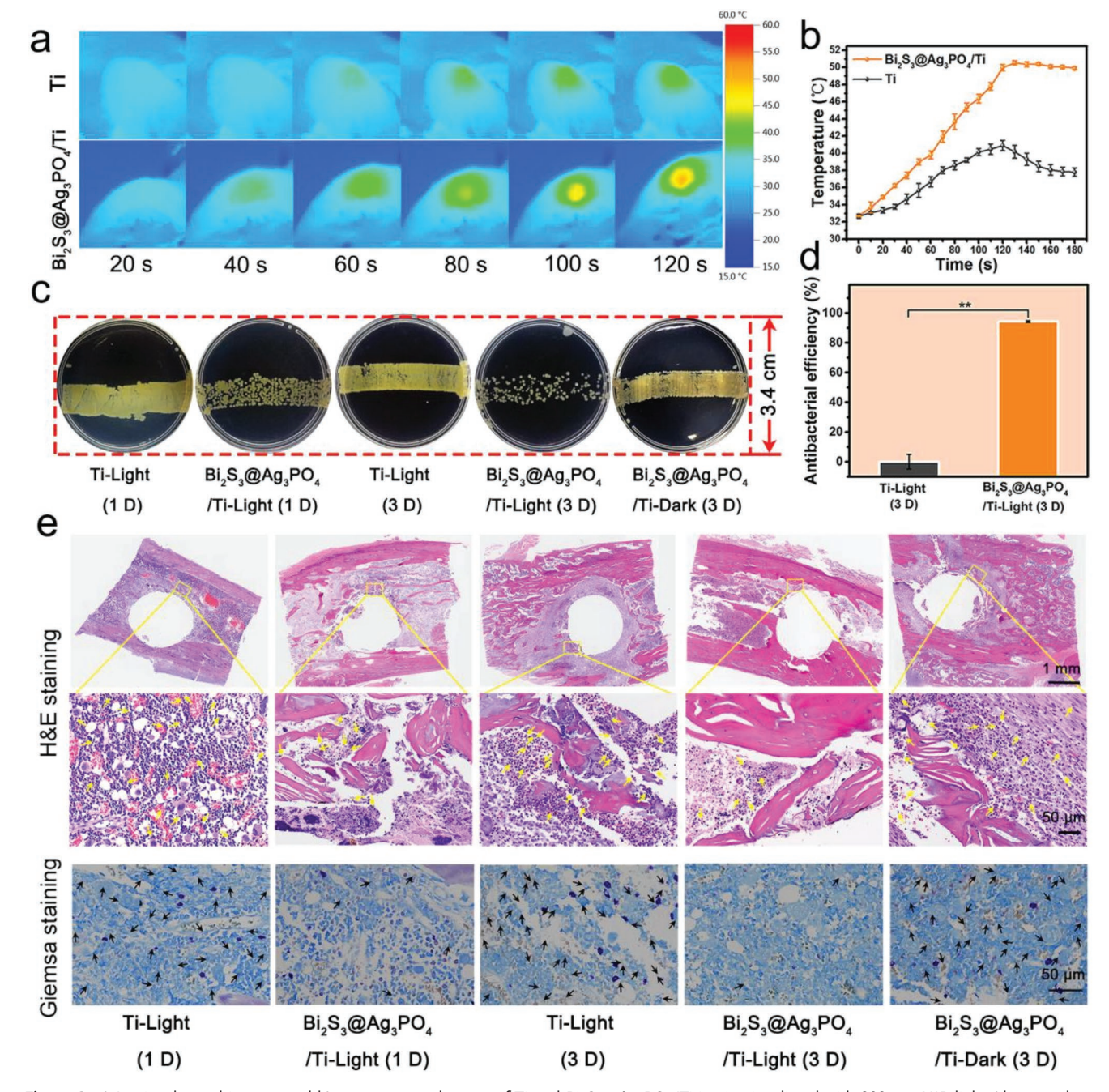


Figure 6. a) In situ thermal images and b) temperature changes of Ti and $Bi_2S_3@Ag_3PO_4/Ti$ in vivo irradiated with 808 nm NIR light (the error bars represent means \pm SD, n = 3). c) Photograph of bacteria colonies. d) Antibiofilm efficiency of Ti-light (3D) and $Bi_2S_3@Ag_3PO_4/Ti$ -light (3D) in vivo in rats after 15 min 808 nm NIR light illumination followed by 3 d feeding, the error bars represent means \pm SD, n = 4: **p < 0.01. e) H&E and Giemsa staining images showing bone tissue infection (neutrophil infiltration and necrotic cells were indicated by yellow arrows, bacteria were indicated by black arrows).

2.6. In Vivo Biofilm Elimination

Considering the good biocompatibility and excellent sterilization ability of the Bi₂S₃@Ag₃PO₄/Ti in vitro, we performed an experiment with *S. aureus* biofilm-infected rats as the model to evaluate antibiofilm efficacy in vivo. **Figure 6**a shows the evolution of in situ photothermal images with irradiation time. Obviously, the temperature of the implant site with Bi₂S₃@Ag₃PO₄/Ti rods increased rapidly with the irradiation time while the

pure Ti group showed little change, which was similar to the results in vitro (Figure S4, Supporting Information). As shown in Figure 6b, after 2 min NIR light (808 nm, 1.5 W cm $^{-2}$) illumination, the temperature increased from 32 to 50 °C, and then maintained at about 50 °C after turning down the light intensity to 1 W cm $^{-2}$. In contrast, the temperature of the pure Ti rod changed little (increased from 32 to 40 °C), and remained at 37 °C even with the same light conditions. These results illustrated that the $\rm Bi_2S_3@Ag_3PO_4/Ti$ exhibited good photothermal

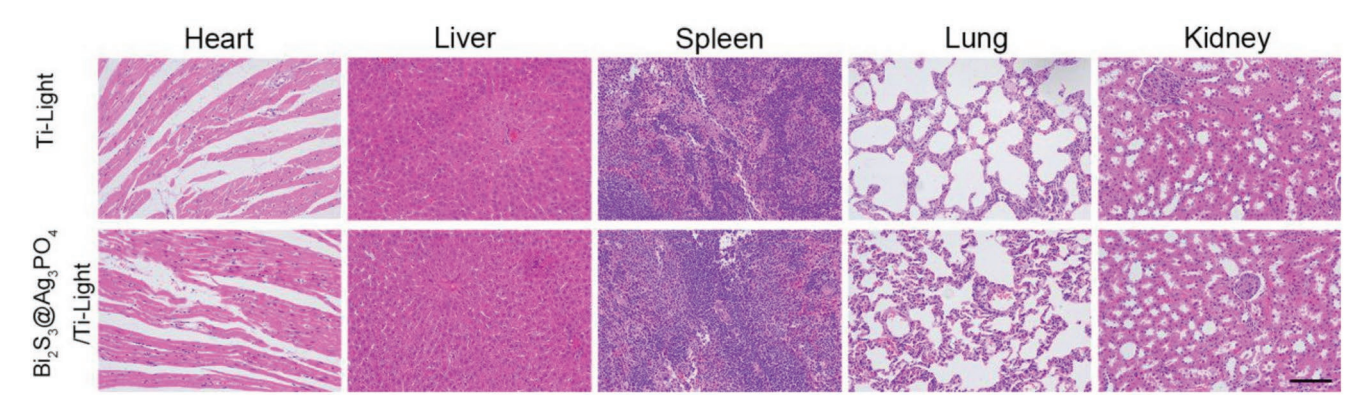


Figure 7. In vivo major organs (heart, liver, spleen, lung, and kidney) H&E staining of rats after 3 d after implant treatment by pure Ti and $Bi_2S_3@Ag_3PO_4/Ti$ (scale bar, 100 μ m).

effects in vivo thanks to the tissue penetration ability of an 808 nm laser NIR light. Figure 6c,d shows the antimicrobial results in vivo. The Ti-light group showed densely stacked colonies, while Bi₂S₃@Ag₃PO₄/Ti-light exhibited sporadic sparse colonies on both the first and third days. It was noted that the bacterial survival rate in the Bi₂S₃@Ag₃PO₄/Ti-light group after 3 d decreased significantly compared to the first day. However, the 3 d plate for the Bi₂S₃@Ag₃PO₄/Ti-dark group showed no antibiofilm effect in vivo. It was deduced that the trace amount of Ag+ released from Bi₂S₃@Ag₃PO₄/Ti did not eliminate bacterial biofilm in vivo in the absence of light, which was consistent with those obtained in vitro. However, after 15 min 808 nm NIR light irradiation, S. aureus biofilm was broken, and then the released Ag+ could collaborate with the immune system to kill the remaining bacteria. The 3 d antimicrobial efficiency calculated from the bacterial plate was 94.30%, which was higher than the one in vitro, because of the released Ag+ from the coating and the immune system of the rats.

Hematoxylin and eosin (H&E) staining was conducted to observe histomorphological changes and evaluate skeletal tissue inflammation and in after phototherapy.[39] As shown in Figure 6e, both the Ti-light (1D/3D) and Bi₂S₃@Ag₂PO₄/Ti-dark (3D) groups exhibited a severe infection induced by biofilm, that is, a high neutrophil infiltration and necrotic cell exudation in H&E stained sections (indicated by yellow arrows). Quantification results of H&E staining in Figure S9 (Supporting Information) indicated inflammatory cell ratios of Ti-light (1D), Ti-light (3D), and Bi₂S₃@Ag₃PO₄/Ti-dark (3D) were 29.00, 25.32, and 24.68%, respectively. However, Bi₂S₃@Ag₃PO₄/Ti-light (1D) showed lower inflammatory cell ratios of 8.13% because the biofilm was eliminated. Therefore, Bi₂S₃@Ag₃PO₄/Ti caused less damage to normal tissue and cells compared to pure Ti. In addition, Bi₂S₃@ Ag₃PO₄/Ti-light (3D) showed the lowest inflammatory cell ratios of 5.53% in skeletal tissue, which indicated Bi₂S₃@Ag₃PO₄/Ti alleviated tissue inflammation and normal tissues and cells were recovering from the damage of biofilm infections, which was similar to previous studies.^[1b,9] Giemsa-stained sections also indicated Bi₂S₃@Ag₃PO₄/Ti-light (3D) host numerous bacteria (indicated by black arrows) on the bone tissues. The results showed that Bi₂S₃@Ag₃PO₄/Ti also exhibited a high bactericidal effect in vivo with NIR light control. As shown in Figure 7, no abnormal effects or damage were observed during histological analysis of

Adv. Healthcare Mater. 2019, 8, 1900835

the heart, liver, spleen, lung, and kidney of rats after 3 d implant treatment by pure Ti and $Bi_2S_3@Ag_3PO_4/Ti$.

3. Conclusions

In summary, we developed an inorganic semiconductor heterojunction photocatalyst of Bi₂S₃@Ag₃PO₄ on a Ti implant that effectively eliminated biofilm within a short time using 808 nm NIR light. The hybrid coating devitalized bacteria rapidly because of the synergistic of photothermal and photocatalysis effect. Compared to Bi₂S₃/Ti, Bi₂S₃@Ag₃PO₄/Ti exhibited higher photocatalytic performance and higher ROS yields. The introduction of Ag₃PO₄ NPs reduced the bandgap of Bi₂S₃/Ti and promoted the separation of photogenerated carriers. Meanwhile, the enlarged surface area was beneficial for photocatalytic interface reactions. In addition, the coating exhibited good cell viability compared to pure Ti. By modifying the surface of bone implants with the NIR-activated nontoxic photocatalyst, we achieved rapid biofilm elimination in situ within 15 min. We hope this practicable strategy of antibiofilm coating might offer new insight on constructing NIR-activated photocatalysts, which will be applied clinically.

Supporting Information

Supporting Information is available from the Wiley Online Library or from the author.

Acknowledgements

All animal experiments were approved by The Department of Orthopedics, Union Hospital, Tongji Medical College, Huazhong University of Science and Technology (Wuhan, China). This work was jointly supported by NSFC (Grant Nos. 51671081, 51871162, and 51801056), the National Key R&D Program of China No. 2016YFC1100600 (sub-project 2016YFC1100604), and Natural Science Fund of Hubei Province (2018CFA064).

Conflict of Interest

The authors declare no conflict of interest.

www.advhealthmat.de

ADVANCED HEALTHCARE MATERIALS

Keywords

 $Bi_2S_3@Ag_3PO_4$ nanorod arrays, biofilm elimination, bone implants, heterostructures, near-infrared photocatalysts

Received: June 27, 2019 Revised: August 15, 2019 Published online: August 28, 2019

- a) D. Campoccia, L. Montanaro, C. R. Arciola, *Biomaterials* 2013, 34, 8018; b) L. Tan, J. Li, X. Liu, Z. Cui, X. Yang, S. Zhu, Z. Li, X. Yuan, Y. Zheng, K. W. K. Yeung, H. Pan, X. Wang, S. Wu, *Adv. Mater.* 2018, 30, 1801808; c) Y. Sun, H. Qin, Z. Yan, C. Zhao, J. Ren, X. Qu, *Adv. Funct. Mater.* 2019, 29, 1808222.
- [2] a) E. D. Brown, G. D. Wright, Nature 2016, 529, 336; b) K. Lewis, Nat. Rev. Drug Discovery 2013, 12, 371.
- [3] H. C. Flemming, J. Wingender, U. Szewzyk, P. Steinberg, S. A. Rice, S. Kjelleberg, Nat. Rev. Microbiol. 2016, 14, 563.
- [4] M. Rybtke, L. D. Hultqvist, M. Givskov, T. Tolker-Nielsen, J. Mol. Biol. 2015, 427, 3628.
- [5] a) Y. Li, X. Liu, L. Tan, Z. Cui, X. Yang, Y. Zheng, K. W. K. Yeung, P. K. Chu, S. Wu, Adv. Funct. Mater. 2018, 28, 1800299; b) P. Hu, T. Wu, W. Fan, L. Chen, Y. Liu, D. Ni, W. Bu, J. Shi, Biomaterials 2017, 141, 86.
- [6] a) G. Liu, S. Zhang, Y. Shi, X. Huang, Y. Tang, P. Chen, W. Si, W. Huang, X. Dong, Adv. Funct. Mater. 2018, 28, 1804317; b) G. Liu, J. Zou, Q. Tang, X. Yang, Y. Zhang, Q. Zhang, W. Huang, P. Chen, J. Shao, X. Dong, ACS Appl. Mater. Interfaces 2017, 9, 40077.
- [7] a) Z. Hou, Y. Zhang, K. Deng, Y. Chen, X. Li, X. Deng, Z. Cheng, H. Lian, C. Li, J. Lin, ACS Nano 2015, 9, 2584; b) Q. Gao, X. Zhang, W. Yin, D. Ma, C. Xie, L. Zheng, X. Dong, L. Mei, J. Yu, C. Wang, Z. Gu, Y. Zhao, Small 2018, 14, 1802290; c) Y. Jiang, P. K. Upputuri, C. Xie, Z. Zeng, A. Sharma, X. Zhen, J. Li, J. Huang, M. Pramanik, K. Pu, Adv. Mater. 2019, 31, 1808166; d) X. Zhen, C. Xie, K. Pu, Angew. Chem., Int. Ed. 2018, 57, 3938.
- [8] F. Faris, M. Thorniley, Y. Wickramasinghe, R. Houston, P. Rolfe, N. Livera, A. Spencer, Clin. Phys. Physiol. Meas. 1991, 12, 353.
- [9] M. Li, L. Li, K. Su, X. Liu, T. Zhang, Y. Liang, D. Jing, X. Yang, D. Zheng, Z. Cui, Z. Li, S. Zhu, K. W. K. Yeung, Y. Zheng, X. Wang, S. Wu, Adv. Sci. 2019, 1900599.
- [10] X. Wang, L. Tan, X. Liu, Z. Cui, X. Yang, K. W. K. Yeung, P. K. Chu, S. Wu, Biomater. Sci. 2018, 6, 2460.
- [11] a) V. Calzia, R. Piras, A. Ardu, A. Musinu, M. Saba, G. Bongiovanni,
 A. Mattoni, J. Phys. Chem. C 2015, 119, 16913; b) Y. Tian, C. F. Guo,
 J. Zhang, Q. Liu, Phys. Chem. Chem. Phys. 2015, 17, 851.
- [12] a) H. Fu, J. Mater. Chem. C 2018, 6, 414; b) F. X. Liang, C. W. Ge, T. F. Zhang, W. J. Xie, D. Y. Zhang, Y. F. Zou, K. Zheng, L. B. Luo, Nanophotonics 2017, 6, 494; c) X. Q. Qiao, Z. W. Zhang, Q. H. Li, D. Hou, Q. Zhang, J. Zhang, D. S. Li, P. Feng, X. Bu, J. Mater. Chem. A 2018, 6, 22580.
- [13] a) S. Wang, X. Li, Y. Chen, X. Cai, H. Yao, W. Gao, Y. Zheng, X. An, J. Shi, H. Chen, Adv. Mater. 2015, 27, 2775; b) M. Y. Malca, H. Bao, T. Bastaille, N. K. Saadé, J. M. Kinsella, T. Friščić, A. Moores, Chem. Mater. 2017, 29, 7766; c) F. P. Ramanery, A. A. P. Mansur, H. S. Mansur, S. M. Carvalho, M. C. Fonseca, Nanoscale Res. Lett. 2016, 11, 187.
- [14] D. Yang, G. Yang, J. Li, S. Gai, F. He, P. Yang, J. Mater. Chem. B 2017, 5, 4152.
- [15] a) M. Zhu, S. Kim, L. Mao, M. Fujitsuka, J. Zhang, X. Wang, T. Majima, J. Am. Chem. Soc. 2017, 139, 13234; b) Z. Guo, S. Zhu, Y. Yong, X. Zhang, X. Dong, J. Du, J. Xie, Q. Wang, Z. Gu, Y. Zhao,

- Adv. Mater. 2017, 29, 1704136; c) X. Wang, J. Xie, C. M. Li, J. Mater. Chem. A 2015, 3, 1235; d) J. Zhou, G. Tian, Y. Chen, Y. Shi, C. Tian, K. Pan, H. Fu, Sci. Rep. 2015, 4, 4027.
- [16] a) Z. Yi, J. Ye, N. Kikugawa, T. Kako, S. Ouyang, H. S. Williams, H. Yang, J. Cao, W. Luo, Z. Li, Y. Liu, R. L. Withers, *Nat. Mater.* 2010, 9, 559; b) X. Xie, C. Mao, X. Liu, L. Tan, Z. Cui, X. Yang, S. Zhu, Z. Li, X. Yuan, Y. Zheng, K. W. K. Yeung, P. K. Chu, S. Wu, *ACS Cent. Sci.* 2018, 4, 724; c) D. J. Martin, G. Liu, S. J. A. Moniz, Y. Bi, A. M. Beale, J. Ye, J. Tang, *Chem. Soc. Rev.* 2015, 44, 7808.
- [17] C. Yang, Y. Chen, W. Guo, Y. Gao, C. Song, Q. Zhang, N. Zheng, X. Han, C. Guo, Adv. Funct. Mater. 2018, 28, 1706827.
- [18] Y. Hongjian, Y. Yong, L. Jianghao, M. Peiyan, W. Yucheng, Z. Fan, F. Zhengyi, J. Mater. Chem. A 2015, 3, 19439.
- [19] T. Wu, X. Zhou, H. Zhang, X. Zhong, Nano Res. 2010, 3, 379.
- [20] Z. Chen, S. Liu, M. Q. Yang, Y. J. Xu, ACS Appl. Mater. Interfaces 2013, 5, 4309.
- [21] Y. Zhang, N. Zhang, Z. R. Tang, Y. J. Xu, ACS Nano 2012, 6, 9777.
- [22] Z. Fang, Y. Liu, Y. Fan, Y. Ni, X. Wei, K. Tang, J. Shen, Y. Chen, J. Phys. Chem. C 2011, 115, 13968.
- [23] M. Li, J. Wang, P. Zhang, Q. Deng, J. Zhang, K. Jiang, Z. Hu, J. Chu, Sci. Rep. 2017, 7, 42484.
- [24] X. Guan, L. Guo, ACS Catal. 2014, 4, 3020.
- [25] J. W. Xu, Z. D. Gao, K. Han, Y. Liu, Y. Y. Song, ACS Appl. Mater. Interfaces 2014, 6, 15122.
- [26] a) Z. Chen, W. Wang, Z. Zhang, X. Fang, J. Phys. Chem. C 2013, 117, 19346; b) A. Raja, A. Chaves, J. Yu, G. Arefe, H. M. Hill, A. F. Rigosi, T. C. Berkelbach, P. Nagler, C. Schüller, T. Korn, C. Nuckolls, J. Hone, L. E. Brus, T. F. Heinz, D. R. Reichman, A. Chernikov, Nat. Commun. 2017, 8, 15251.
- [27] V. Etacheri, M. K. Seery, S. J. Hinder, S. C. Pillai, Chem. Mater. 2010, 22, 3843.
- [28] L. Liu, Y. Qi, J. Lu, S. Lin, W. An, Y. Liang, W. Cui, Appl. Catal., B 2016, 183, 133.
- [29] a) Y. Li, W. Zhang, J. Niu, Y. Chen, ACS Nano 2012, 6, 5164.;
 b) C. Liu, D. Kong, P. C. Hsu, H. Yuan, H. W. Lee, Y. Liu, H. Wang, S. Wang, K. Yan, D. Lin, P. A. Maraccini, K. M. Parker, A. B. Boehm, Y. Cui, Nat. Nanotechnol. 2016, 11, 1098;
 c) J. Li, X. Liu, L. Tan, Y. Liang, Z. Cui, X. Yang, S. Zhu, Z. Li, Y. Zheng, K. W. K. Yeung, X. Wang, S. Wu, Small Methods 2019, 3, 1900048.
- [30] H. Y. Jiang, P. Zhou, Y. Wang, R. Duan, C. Chen, W. Song, J. Zhao, Adv. Mater. 2016, 28, 9776.
- [31] D. F. Laine, A. Blumenfeld, I. F. Cheng, Ind. Eng. Chem. Res. 2008, 47, 6502.
- [32] a) Y. Yamakoshi, N. Umezawa, A. Ryu, K. Arakane, N. Miyata, Y. Goda, T. Masumizu, T. Nagano, J. Am. Chem. Soc. 2003, 125, 12803; b) H. Goto, Y. Hanada, T. Ohno, M. Matsumura, J. Catal. 2004, 235, 232
- [33] R. Roy, M. Tiwari, G. Donelli, V. Tiwari, Virulence 2018, 9, 522.
- [34] a) K. Ai, Y. Liu, J. Liu, Q. Yuan, Y. He, L. Lu, Adv. Mater. 2011, 23, 4886; b) B. Roy, A. P. Chattopadhyay, A. Samadder, A. R. Khuda Bukhsh, J. Sol-Gel Sci. Technol. 2016, 77, 446.
- [35] C. R. Chen, H. Y. Zeng, M. Y. Yi, G. F. Xiao, S. Xu, S. G. Shen, B. Feng, Appl. Catal., B 2019, 252, 47.
- [36] J. Liu, X. Zheng, L. Yan, L. Zhou, G. Tian, W. Yin, L. Wang, Y. Liu, Z. Hu, Z. Gu, C. Chen, Y. Zhao, ACS Nano 2015, 9, 696.
- [37] M. Zhang, H. Cheng, Z. Gong, J. Zhang, X. Liu, B. Wang, L. Ban, Y. Zeng, Z. Zhu, Adv. Funct. Mater. 2017, 27, 1703932.
- [38] a) G. Jin, H. Qin, H. Cao, S. Qian, Y. Zhao, X. Peng, X. Zhang, X. Liu, P. K. Chu, Biomaterials 2014, 35, 7699; b) H. Cao, W. Zhang, F. Meng, J. Guo, D. Wang, S. Qian, X. Jiang, X. Liu, P. K. Chu, ACS Appl. Mater. Interfaces 2017, 9, 5149.
- [39] J. Li, L. Tan, X. Liu, Z. Cui, X. Yang, K. W. K. Yeung, P. K. Chu, S. Wu, ACS Nano 2017, 11, 11250.